PCCP

PAPER

View Article Online
View Journal | View Issue

Cite this: *Phys. Chem. Chem. Phys.*, 2024, **26**, 18368

Stereodynamical control of cold HD + D_2 collisions†

Bikramaditya Mandal, [a] James F. E. Croft, [b] Pablo G. Jambrina, [c] Hua Guo, [d] F. Javier Aoiz [e] and Naduvalath Balakrishnan *[a]

Received 26th April 2024,
Accepted 27th May 2024

DOI: 10.1039/d4cp01737d

rsc.li/pccp

We report full-dimensional quantum calculations of stereodynamic control of HD(v = 1, j = 2) + D_2 collisions that has been probed experimentally by Perreault *et al.* using the Stark-induced adiabatic Raman passage (SARP) technique. Computations were performed on two highly accurate full-dimensional H_4 potential energy surfaces. It is found that for both potential surfaces, rotational quenching of HD from $j_{HD} = 2 \rightarrow j'_{HD} = 0$ with concurrent rotational excitation of D_2 from $j_{D_2} = 0 \rightarrow j'_{D_2} = 2$ is the dominant transition with cross sections four times larger than that of elastically scattered $D_2\left(j_{D_2} = j'_{D_2} = 0\right)$ for the same quenching transition in HD. This process was not considered in the original analysis of the SARP experiments that probed $\Delta j_{HD} = -2$ transitions in HD(v_{HD} = 1, j_{HD} = 2) + D_2 collisions. Cross sections are characterized by an l = 3 resonance for *ortho*-D_2(j_{D_2} = 0) collisions, while both l = 1 and l = 3 resonances are observed for the *para*-D_2(j_{D_2} = 1) partner. While our results are in excellent agreement with prior measurements of elastic and inelastic differential cross sections, the agreement is less satisfactory with the SARP experiments, in particular for the $j_{HD} = 2 \rightarrow j'_{HD} = 0$ transition for which the theoretical calculations indicate that D_2 rotational excitation channel is the dominant inelastic process.

1 Introduction

Inelastic and reactive collisions of small molecules have received much interest due to their importance in the chemistry of the early universe,[1–7] Earth's atmosphere, interstellar media (ISM),[4,8,9] and star formation regions.[10–12] Being the most abundant molecule in astrophysical environments, H_2 and its isotopic counterparts HD and D_2, were a major focus of experimental and theoretical studies.[1,13] Unlike H_2 which lacks a permanent dipole moment, which makes its detection more challenging, the isotopologue HD possesses a non-zero dipole moment.[4,13] The signatures of $j = 1 \rightarrow j' = 0$ rotational transition in HD were observed by the Herschel space observatory[14,15] and by the long wavelength spectrometer at the Infrared space observatory (ISO).[16,17] The prospects of detecting the $j = 4 \rightarrow j' = 3$ transition in HD by the Atacama large millimeter array (ALMA),[18] as well as other transitions by the Spitzer space telescope[16,19] have led to much interest in collisions of rotationally excited HD. Due to its small dipole moment the HD molecule is also thought to play an important role in the cooling of the primordial gas despite its relatively small abundance compared to H_2.[1,4,13,20,21] Major advancements in *ab initio* electronic structure calculations in the last decade, coupled with high-performance computing and machine-learning algorithms have led to the availability of high quality potential energy surfaces (PESs) for the interaction between two H_2 molecules.[22–24] These surfaces have formed the basis of a number of full-dimensional quantum calculations of H_2–H_2 and H_2–HD collisions of interest in astrophysics.[4,5,13,25] Very recently, a full-dimensional PES for the H_4 system that accounts for four-center exchange reactions and collision-induced dissociation channels in H_2 + H_2 collisions have also been reported.[26]

Recent advances in molecular cooling and trapping technologies have also led to renewed interest in inelastic and reactive collisions of atom–molecule and molecule–molecule systems. Indeed, collisions of cold and ultracold diatomic molecules are an active area of experimental and theoretical research due to their applications to quantum sensing, ultracold chemistry, quantum computing, and quantum information processing.[27–43]

[a] *Department of Chemistry and Biochemistry, University of Nevada, Las Vegas, Nevada 89154, USA. E-mail: naduvala@unlv.nevada.edu*
[b] *Department of Chemistry, Durham University, South Road, Durham, DH1 3LE, UK*
[c] *Departamento de Química Física, University of Salamanca, Salamanca 37008, Spain*
[d] *Department of Chemistry and Chemical Biology, University of New Mexico, Albuquerque, New Mexico 87131, USA*
[e] *Departamento de Química Física, Universidad Complutense, Madrid 28040, Spain*

† Electronic supplementary information (ESI) available: Stereodynamical control of cold HD + D_2 collisions. It includes similar results as those presented in the main text but obtained using the full-dimensional H_4 PES by Hinde. Also, contour plots of differential cross sections for the H-SARP and V-SARP preparations as a function of the collision energy and scattering angle are included. See DOI: https://doi.org/10.1039/d4cp01737d

Molecular collisions in this regime are characterized by large de Broglie wavelengths and are strongly influenced by long-range intermolecular forces. Although, diatomic species such as CaF, SrF, RbCs, KRb, NaK, *etc.* are preferred molecules for such applications,[44–48] their small rotational constants lead to high densities of states making rigorous quantum calculations of diatom–diatom collisions involving these molecules computationally intractable.[43,49,50] Therefore, lighter diatomic molecules, such as H_2 and its isotopologues, are generally preferred to benchmark theoretical studies against experiments. These systems are characterized by large rotational constants and low densities of states, thus requiring only a small number of orbital angular momentum partial waves to yield converged cross sections in the 1 kelvin range of collision energies.[43]

Zare and coworkers have recently developed a coherent optical technique, called Stark-induced adiabatic Raman passage (SARP), to study quantum controlled cold collisions of light molecular systems, such as H_2, HD and D_2.[51–63] The SARP technique allows preparation of a phase-coherent superposition of degenerate alligned states (m_j) within a single ro-vibrational state.[64] Additionally, the colliding partners are adiabatically expanded and co-propagated in the same molecular beam, yielding relative collision energies in the 1 kelvin regime for collisions involving H_2 and its isotopologues. This provides a powerful approach to probe stereodynamics in collision of quantum state-prepared and aligned molecules.[65] The SARP technique has recently been extended to chemical reactions of state-prepared HD with H atoms leading to the D + H_2 product using a crossed molecular beam technique but at thermal and superthermal collision energies or collision energies above 0.5 eV.[66]

Zare, Mukherjee and collaborators have published a series of papers applying the SARP technique to rotational quenching of HD and D_2 by collisions with H_2, D_2, and He.[51–63] These systems are amenable to full-dimensional quantum calculations and allow direct comparisons between theory and experiment. Their first experiment involved rotational quenching of aligned HD prepared in the $v = 1, j = 2$ initial state colliding with unpolarized D_2.[53,63] Subsequent studies involved colliding partners of H_2,[53] D_2,[63] and He,[58,60] all of which were unprepared (unpolarized). They also applied the SARP technique to D_2 + He[55,57] and D_2 + Ne collisions.[56] In their most recent work rotational quenching in collisions of two aligned D_2 molecules prepared in the $v = 2, j = 2$ initial state[61] was reported.

The SARP experiments stimulated a series of theoretical studies aimed at gaining more insight into the quantum dynamics and relevant partial waves that control the collision outcome.[23,31,43,67–73] Quantum dynamical studies of stereodynamic control of reactive collisions of F + HD[74] and H + D_2/D + HD[75] systems have also been reported recently. While analysis of the experimental data and the experimental relative velocity distribution can discern the relevant partial waves involved in the collision dynamics, theoretical studies are needed to identify specific partial-wave resonances that control the collision outcome. Theory is particularly useful as the experimental measurements were not done with energy resolution, and averaging over the relative collision energy is needed.

Theoretical investigations of HD + H_2,[68,73] HD + He,[69,70] D_2 + D_2,[43,71] and D_2 + He[72] yielded results in reasonable agreement with experiments for the angular distribution though assignments of specific resonances that contribute to signatures of the measured angular distribution differed between theory and experiment. This is due in part to the lack of energy resolution in the experiment. Though the HD + D_2 system was the topic of the first SARP experiment by Perreault *et al.*,[53] no theoretical studies have been reported so far. For this system experimental data was reported for both $\Delta j_{HD} = -1$ and -2 transitions with HD prepared initially in the $v_{HD} = 1, j_{HD} = 2$ state, while the D_2 molecule is unprepared.[53,54] The measured angular distributions of the HD molecule for the $v'_{HD} = 1, j'_{HD} = 0$ and $v'_{HD} = 1, j'_{HD} = 1$ final states involve a convolution of relative collision energies in the 1 mK–10 K range with the peak of the energy distribution centered around 1 K. Here, we report the first theoretical study of this process using full-dimensional quantum scattering calculations on two highly accurate interaction potentials for the H_2–H_2 system.[22,23] Besides its importance in astrophysics, this system also serves as a benchmark for inelastic diatom–diatom collisions.

The article is organized as follows: Section II provides a brief description of the two potential energy surfaces, quantum scattering methods, and the SARP preparation. A detailed discussion of our findings, state-to-state cross sections, partial wave analysis, and comparisons between theory and experiments are provided in Section III. Finally, in Section IV, we summarize the key findings.

2 Methods

2.1 Potential energy surface

The H_4 system is the simplest neutral four atom system; so high quality full-dimensional PESs are available for this molecular system.[22–24] In this study, we adopt the PESs by Zuo, Croft, Yao, Balakrishnan, and Guo (ZCYBG)[23] and by Hinde[22] (hereafter referred to as the ZCYBG PES and Hinde PES, respectively). A detailed comparison between the two surfaces was reported in previous studies and is not our focus here.[23,43] The interaction potential is represented in Jacobi coordinates (R, r_1, r_2, θ_1, θ_2, ϕ_{12}) where R is the center-of-mass (COM) separation between the two molecules, r_1 and r_2 are the two diatomic vibrational coordinates, θ_1 and θ_2 are the two Jacobi angles of $\vec{R}$ with $\vec{r}_1$ and $\vec{r}_2$, and ϕ_{12} is the dihedral angle. The current system of interest, HD–D_2, has the same interaction potential as the H_2–H_2 system within the Born–Oppenheimer approximation, except that the COM of the HD molecule is shifted compared to the H_2 COM. Thus, the interaction potential for HD + D_2 is expressed in this coordinate system as described in our prior studies of HD + H_2 collisions.[4,5]

The angular dependence of the PESs was parameterized by the following spherical harmonic expansion as described in detail elsewhere:[23,43]

$$V\left(\vec{r}_1, \vec{r}_2, \vec{R}\right) = \sum_{\lambda_1,\lambda_2,\lambda_{12}} C_{\lambda_1,\lambda_2,\lambda_{12}}(r_1, r_2, R)\, Y_{\lambda_1,\lambda_2,\lambda_{12}}\left(\hat{r}_1, \hat{r}_2, \hat{R}\right) \quad (1)$$

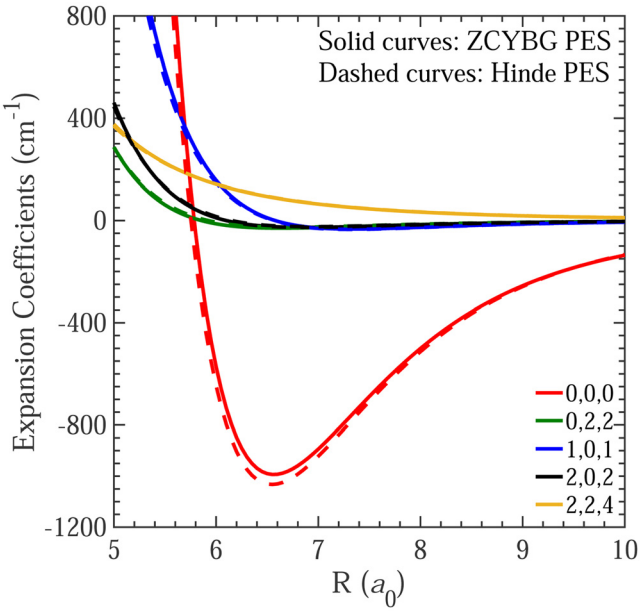

Fig. 1 The dominant expansion terms in the angular dependence of the HD–D_2 PESs as a function of the intermolecular separation. The solid curves represent the results from the ZCYBG PES,[23] while dashed curves are obtained using the Hinde PES.[22] The numbers in the legends correspond to λ_1, λ_2, and λ_{12}, respectively.

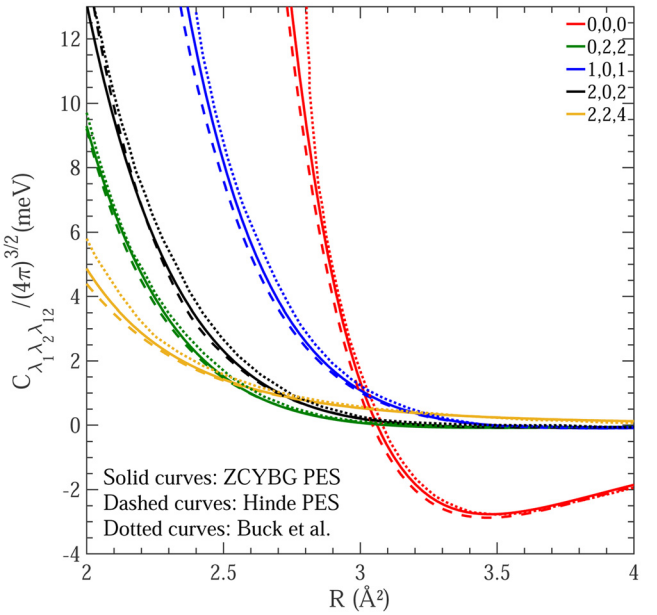

Fig. 2 Same as Fig. 1. In addition to the solid curves obtained from the ZCYBG PES[23] and dashed curves from the Hinde PES,[22] the dotted curves show available results using the M80 PES reported by Buck *et al.*[76] Note the different units for the energy and R compared to Fig. 1.

where,

$$Y_{\lambda_1,\lambda_2,\lambda_{12}}(\hat{r}_1,\hat{r}_2,\hat{R}) = \sum_{m_1,m_2,m_{12}} \langle \lambda_1 m_1 \lambda_2 m_2 | \lambda_{12} m_{12} \rangle \times Y_{\lambda_1,m_1}(\hat{r}_1) Y_{\lambda_2,m_2}(\hat{r}_2) \times Y^*_{\lambda_{12},m_{12}}(\hat{R}). \quad (2)$$

First, we present a brief comparison between the two PESs. Fig. 1 displays the five leading terms in the angular dependence of the interaction potential obtained from the ZCYBG PES (solid lines) and the Hinde PES (dashed lines) with the HD and D_2 bond lengths fixed at their equilibrium value of r_e = 1.401 a_0. The isotropic term derived from the ZCYBG and Hinde PESs is found to be about 993 cm^{-1} and 1032 cm^{-1} deep, respectively, at a HD–D_2 COM separation of R = 6.55 a_0 ($\sim$3.47 Å). We also compare the five leading expansion terms ($C_{\lambda_1,\lambda_2,\lambda_{12}}$) with a previous study available in the literature from 1980s by Buck *et al.*[76,77] In their joint theory-experiments, Buck *et al.* adopted an *ab initio* PES, named M80, to derive the expansion coefficients using an expression similar to eqn (1). The comparison is provided in Fig. 2 in the same energy units reported by Buck *et al.*[76,77] As Fig. 2 illustrates, the expansion terms are in excellent agreement with both PESs used in this work. The potential minimum for the isotropic terms for all three potentials occurs at an intermolecular separation of $R \sim$ 3.5 Å. The well-depth of the isotropic term differs by about 0.46% and 3.46% compared to the ZCYBG PES and Hinde PES, respectively. The isotropic, leading anisotropic, and other terms show maximum deviation in the highly repulsive region, not sampled at low and moderate collision energies.

For the scattering calculations of HD + D_2, it was found that $\lambda_1 \leq 2$ and $\lambda_2 \leq 6$ for HD and D_2, respectively, were sufficient to yield converged results for both the ZCYBG and Hinde PESs.

2.2 Scattering calculations

Full-dimensional quantum scattering calculations were carried out using a modified version of the TwoBC code.[78] The methodology for rovibrational scattering of two $^1\Sigma$ diatomic molecules is well established, and several benchmark calculations of the H_2–H_2 system and its isotopic variants have been reported in the literature.[5,79–82] Here we provide a brief outline to introduce the necessary quantum numbers and parameters involved in the calculations. A time-independent quantum approach within the close-coupling method is used for the scattering calculations.[82] This yields the scattering matrix, **S**, from which observable quantities are calculated. To label the initial and final states, we introduce the combined molecular state (CMS), $n \equiv v_1 j_1 v_2 j_2$ where v_1 and j_1 are the initial vibrational and rotational quantum numbers of asymptotic channels for the HD molecule while v_2 and j_2 denote the same for D_2. Similarly, we define $n' \equiv v'_1 j'_1 v'_2 j'_2$ for the final channels of HD and D_2. The state-to-state integral cross section (ICS) for ro-vibrationally inelastic scattering at a collision energy E_c is given by

$$\sigma_{n\to n'}(E_c) = \frac{\pi}{k_n^2 (2j_1+1)(2j_2+1)} \sum_{J,j_{12},j'_{12},l,l'} (2J+1) \left| T^J_{n,l,j_{12},n',l',j'_{12}} \right|^2 \quad (3)$$

where, $k_n{}^2 = 2\mu E_c/\hbar^2$, $E_c = E - E_n$ where E is the total energy and E_n is the asymptotic energy of channel n, μ is the reduced mass

of the combined molecular system of HD + D_2, and $T^J = 1 - S^J$. The quantum number J refers to the total angular momentum $\mathbf{J} = \mathbf{l} + \mathbf{j_{12}}$, l is the quantum number for the orbital angular momentum $\mathbf{l}$, and the total molecular rotational angular momentum $\mathbf{j_{12}} = \mathbf{j_1} + \mathbf{j_2}$.

The differential cross section (DCS) is given in terms of the scattering amplitude q as a function of the scattering angle, θ and the azimuthal angle ϕ. The θ dependence of the scattering amplitude is evaluated within the helicity representation, as given by Schaefer and Meyer:[83]

$$q_{n,m\to n',m'}(\theta) = \frac{1}{2k_n}\sum_J (2J+1) \sum_{j_{12},j'_{12},l,l'} i^{l-l'+1} T^J_{n,l,j_{12},n',l',j'_{12}} d^J_{m_{12},m'_{12}}(\theta) \times \langle j_{12} m_{12} J - m_{12} | l 0\rangle \langle j'_{12} m'_{12} J - m'_{12} | l' 0\rangle \times \langle j_1 m_1 j_2 m_2 | j_{12} m_{12}\rangle \langle j'_1 m'_1 j'_2 m'_2 | j'_{12} m'_{12}\rangle \quad (4)$$

where $d^J_{m_{12},m'_{12}}(\theta)$ is an element of the Wigner reduced rotation matrix, $m \equiv m_1, m_2, m_{12}, m' \equiv m'_1, m'_2, m'_{12}$, and the quantities in angular brackets $\langle \ldots . | .. \rangle$ are Clebsch–Gordan coefficients. For isotropic collisions, the differential rovibrational state resolved cross sections are obtained by summing over all final m'-states and averaging over initial m-states as given below:

$$\frac{d\sigma_{n\to n'}}{d\Omega} = \frac{1}{(2j_1+1)(2j_2+1)} \sum_{m,m'} \left| q_{n,m\to n',m'} \right|^2 \quad (5)$$

where $d\Omega = \sin\theta d\theta d\phi$ is the solid angle.

The expressions given above for integral and differential cross sections assume that the colliding entities are unpolarized. In the SARP experiments of Perreault *et al.*, rotational quenching of HD by D_2 was explored by controlling the alignment of HD relative to the SARP laser polarization.[53,54] This is achieved by selecting appropriate m_j components of the rotational state j of the HD molecule relative to the polarization of the SARP laser.[84,85] A rotational state of the HD molecule $|j,\tilde{m}\rangle$ prepared by the SARP method can be expressed as

$$\sum_{m_j=-j_{HD}}^{j_{HD}} d^{j_{HD}}_{\tilde{m},m_j}(\beta) \left| j_{HD}, m_j \right\rangle \quad (6)$$

where β is the angle between the initial beam velocity and the initial polarization of the laser, *i.e.*, the alignment angle. In the SARP experiments studied here, only the $\tilde{m} = 0$ preparation is considered. An angle $\beta = 0^\circ$ corresponds to a horizontal alignment of the molecular bond axis with respect to the initial velocity vector. This is referred to as the H-SARP preparation, and for the HD molecule in the $j = 2$ rotational state, it corresponds to $|j = 2, m_j = 0\rangle$ initial state. For the same $j = 2$ rotational state of the HD molecule, a vertical alignment of the HD bond axis corresponding to $\beta = \frac{\pi}{2}$, known as V-SARP, includes a superposition of m_j states given by

$$\sqrt{\frac{3}{8}} |j = 2, m_j = +2\rangle - \frac{1}{2} |j = 2, m_j = 0\rangle + \sqrt{\frac{3}{8}} |j = 2, m_j = -2\rangle. \quad (7)$$

In the HD + D_2 experiments of Perreault *et al.*,[53,54] both H-SARP and V-SARP preparations of the HD molecule were realized for the initial rovibrational state of $v_{HD} = 1, j_{HD} = 2$. The corresponding DCSs for the SARP preparations are given by

$$\frac{d\sigma_{n\to n'}(\beta)}{d\Omega} = \frac{1}{(2j_2+1)} \sum_{m_1,m_2,m'_1,m'_2} \left| d^{j_{HD}}_{0,m_1}(\beta) \right|^2 \left| q_{n,m\to n',m'} \right|^2, \quad (8)$$

where the redundant indices m_{12} and m'_{12} are omitted in the summation. Note that the experimental results correspond to an integration over the azimuthal angle which washes out any interference between different m_1 states in the initial preparation.[67,71] Thus, the overall effect of the initial alignment is captured by the weight factor $\left| d^{j_{HD}}_{0,m_1}(\beta) \right|^2$ attached to each $|q|^2$ term for a given m_1.

In the computations, a basis set including three vibrational levels v = 0–2 was considered for both molecules. For the HD molecule, within each vibrational level six rotational states j = 0–6 were included while for the D_2 molecule three rotational states, j = 0, 2, and 4 were considered, which led to nearly 200 CMSs. Calculations were done for total angular momentum quantum numbers J = 0–8. The coupled-channel equations resulting from the time-independent Schrödinger equation were integrated from R = 3 to R = 103 a_0 with a step size of $\Delta R = 0.05\ a_0$. This choice of parameters yield results converged to within 1% in the collision energy regime of 1 mK to 10 K reported here. Additional calculations were carried out at higher collision energies to compare against the experimental and theoretical results of Buck *et al.*[76,77] as discussed in the next section. These calculations adopted the same rotational basis sets for both molecules but limited to the v = 0 vibrational level.

3 Results

3.1 Comparisons with prior theory and experimental results

First, we benchmark our results against available experimental and theoretical results. Unfortunately, very limited data exist for this system and the available experimental and theoretical results correspond to the work of Buck *et al.*[76,77] four decades ago. The measurements were reported at collision energies of 45.4 meV ($\sim$527 K) and 70.3 meV ($\sim$816 K)[76,77] and the corresponding theoretical calculations adopted a rigid rotor formalism for both molecules. Because the previous calculations and measurements correspond to fairly high collision energies we include total angular momentum quantum number J up to 80 to achieve a convergence within 1% with respect to summation over J. Fig. 3 shows a comparison of DCS from our calculation for both elastic and inelastic collisions on the ZCYBG PES with the theoretical results of Buck *et al.* at collision energies of 45.4 and 70.3 meV. Our results correspond to both molecules in the ground

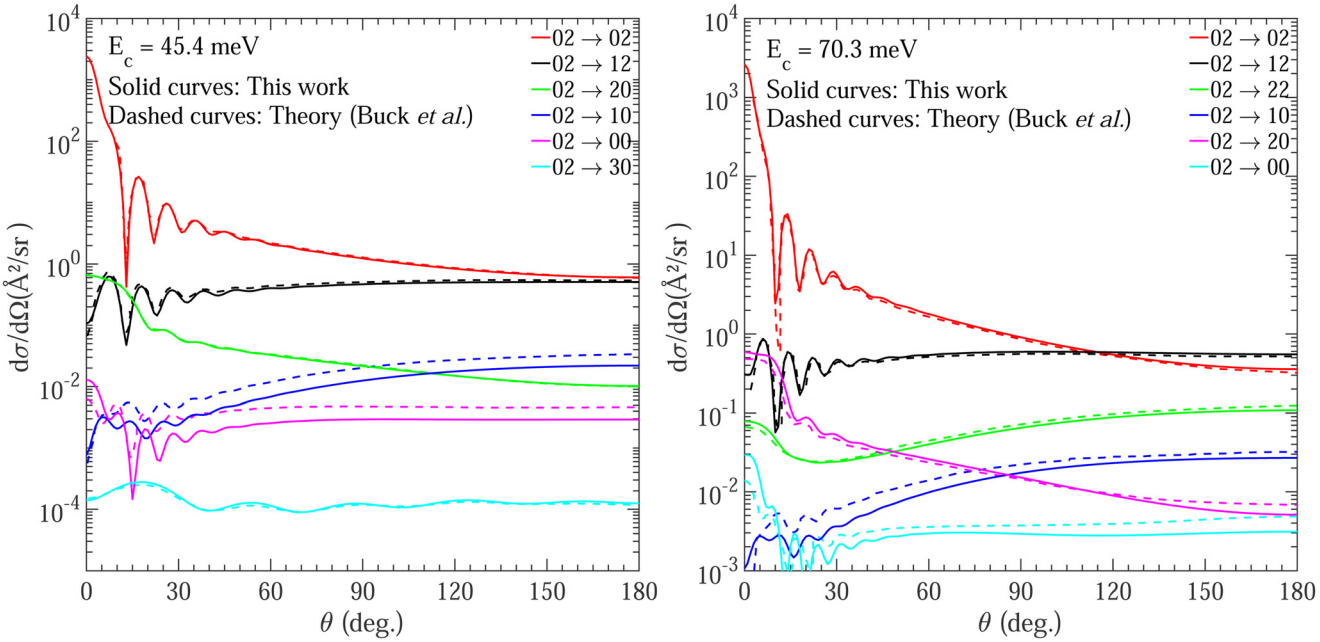

Fig. 3 Comparison of angular dependence of the calculated differential cross sections from the present study using the ZCYBG PES (solid curves) and those of Buck *et al.* (dashed curves) for state-to-state transitions (refer to the legends inside figure) for two collision energies, 45.4 meV (left panel) and 70.3 meV (right panel). The transitions are denoted as $j_{HD}j_{D_2} \rightarrow j'_{HD}j'_{D_2}$.

vibrational state. Similar comparisons using the Hinde PES are provided in the ESI.† The agreement between the two results is excellent for both collision energies for the entire range of scattering angle despite the large variation in the magnitude of the DCS for the different transitions. It is remarkable to see the oscillatory behavior of the DCS arising from interference between different partial wave contributions quantitatively reproduced by the two calculations. The DCSs for the elastic transition, 02→02 and the dominant inelastic transition, namely 02→12 (where the numbers denote j_{HD} j_{D_2} before and after collision; see figure caption for the notation), are almost identical from the two calculations for both collision energies. Slight differences seen

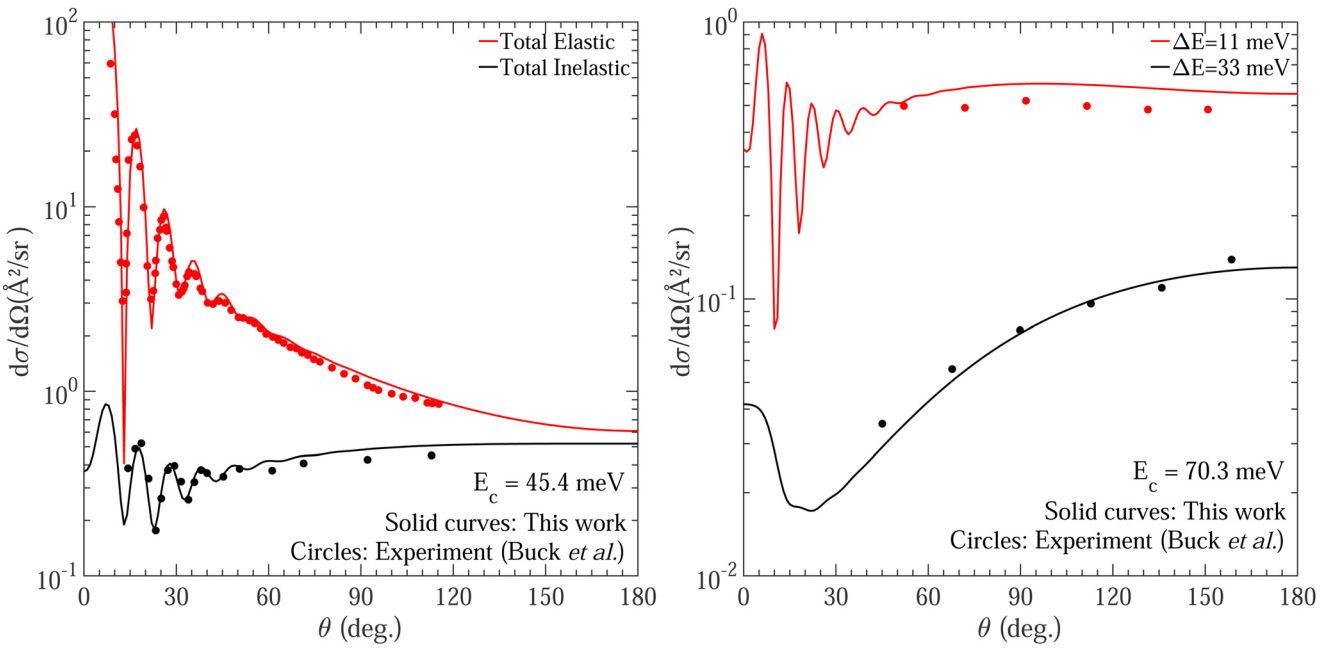

Fig. 4 Comparison of angular dependence of the total elastic and inelastic differential cross sections between our calculations using the ZCYBG PES (solid curves) and experimental data of Buck *et al.* (circles) for two collision energies, 45.4 meV (left panel) and 70.3 meV (right panel). The total elastic and inelastic cross sections in the left panel and that for ΔE = 11 meV and ΔE = 33 meV in the right panel are obtained by taking weighted sum of ICSs for different thermally populated D_2 initial rotational states as described in more details in the text.

for the weaker 02 → 10 and 02 → 00 transitions can be attributed to differences in the potential expansion term $\lambda_{2,0,2}$ as illustrated in Fig. 2. However, even for these weaker transitions with 2–3 orders of magnitude smaller DCSs than the elastic and leading inelastic transitions, the oscillatory behavior as a function of the scattering angle is nearly identical in both calculations.

In Fig. 4 we compare our DCS results on the ZCYBG PES with the experimental results of Buck *et al.*[76] for the two collision energies of 45.4 and 70.3 meV. A similar comparison for the Hinde PES is provided in the ESI.† To compare with the experimental results, we used the same procedure as in Buck *et al.*[77] where we summed over contributions from different thermally populated rotational levels of the D_2 collision partner. The total elastic cross sections in the left panel at a collision energy of 45.4 meV were obtained by taking a weighted sum of transitions $j_{HD}j_{D_2} \rightarrow j'_{HD}j'_{D_2}$ for 00 → 00, 01 → 01, 02 → 02 with weights 0.27, 0.33 and 0.40 for D_2 rotational states j = 0, 1, and 2, respectively. Similarly, the total inelastic cross sections were obtained by a weighted sum of the transitions 00 → 10, 01 → 11, 02 → 12, and 02 → 20. For details, see Buck *et al.*[76,77] In the right panel of Fig. 4, the filled circles represent the experimental data, while the solid curves show our results. Here, ΔE refers to the energy difference between the combined molecular states of HD + D_2. Specifically, ΔE = 11 meV includes transitions 02 → 20, 00 → 10, 01 → 11, and 02 → 12 while ΔE = 33 meV includes 00 → 20, 01 → 21, 02 → 22, and 00 → 12. The total cross sections corresponding to the energy gaps are then obtained by taking a weighted sum of D_2 rotational states j = 0, 1 and 2 with weights of 0.62, 0.33, and 0.05, respectively. The agreement is excellent, for both elastic and inelastic collisions, including scattering angles where the DCS shows strong oscillatory pattern. The excellent agreement between our results and the theoretical and experimental results of Buck *et al.* at the level of differential cross sections validates the accuracy of the results presented here and the quality of the PESs adopted for the scattering calculations.

3.2 Sensitivity of low-energy collisions to potential energy surfaces

The experimental data by Perreault *et al.*[53,54] corresponds to pure rotational quenching of the HD molecule from $j_{HD} = 2 \rightarrow j'_{HD} = 0, 1$ within the v_{HD} = 1 vibrational level in collisions with n-$D_2(v_{D_2} = 0)$ but with a thermal population of rotational levels. Since the D_2 molecules were used without state preparation D_2 is considered as an isotropic collision partner. The experiment involves a broad distribution of collision energies centered around ∼1 K with the higher energy tail extending to about ∼8 K. To what extent energies below 1 K contribute to the measured angular distribution is not clear but we first explore sensitivity of rotationally inelastic cross sections to the interaction potential at collision energies relevant to the experiment. Fig. 5 shows the integral cross-section as a function of the collision energy for the $j_{HD} = 2 \rightarrow j'_{HD} = 0$ transition for $j_{D_2} = j'_{D_2} = 0$. Results are presented for both the Hinde and ZCYBG PESs. As shown in the figure the newer ZCYBG PES

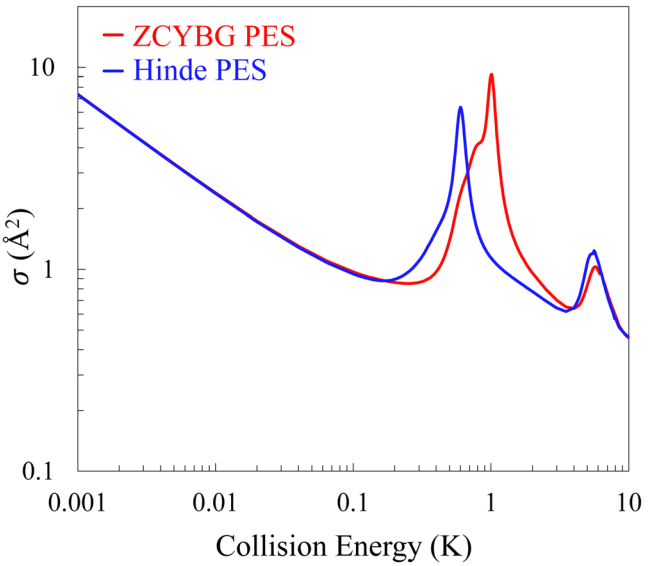

Fig. 5 Integral cross sections for $j_{HD} = 2 \rightarrow j'_{HD} = 0$ transition in HD + D_2 collisions within the v_{HD} = 1 vibrational level for $j_{D_2} = j'_{D_2} = 0$ as a function of the collision energy. The results obtained on the ZCYBG PES are shown by the red solid curve while those on the Hinde PES are denoted by the blue curve.

predicts slightly higher values of cross sections, ∼9 Å^2 near the peak of the primary resonance at about ∼1 K compared to ∼6 Å^2 on the Hinde PES. Also, the resonance occurs at about 1.01 K for the ZCYBG PES compared to 0.62 K for the Hinde PES, which is also narrower. In contrast, the Hinde PES yields slightly higher values (less than 0.2 Å^2) of the cross section for the secondary resonance at 5.6 K even though the resonance energy differs by only ∼0.1 K for the two PESs. Apart from these differences in the resonance region, it is striking to note that the background cross section, including the ultracold *s*-wave limit, is nearly identical for both PESs. We note that below ∼10 mK, the cross sections exhibit the well-known Wigner threshold behavior where they vary inversely as the velocity or $1/\sqrt{E_c}$.[86,87] Such resonance features supported by the entrance channel van der Waals potentials have been reported for many atom–diatom and diatom–diatom systems, including the benchmark F + H_2 and F + HD chemical reactions.[88,89] The properties of these resonances are generally very sensitive to the choice of the interaction potential, in particular, if they occur close to the entrance channel threshold.[72,88,89]

A partial wave analysis of the cross sections for the $j_{HD} = 2 \rightarrow j'_{HD} = 0$ transition shows that the primary peak corresponds to an l = 3 shape resonance originating from total angular momentum quantum number J = 3. The partial wave resolved cross sections on the ZCYBG PES is shown in Fig. 6. The shoulder feature seen on the left side of the primary resonance peak also arises from l = 3 but from J = 5. A similar analysis on the Hinde PES is shown in the ESI† that also features an l = 3 resonance for the primary peak. The secondary resonance corresponds to l = 4 arising from J = 2, 4, and 6 coinciding with the same collision energy on both the PESs.

Fig. 7 shows integral cross sections for the $\Delta j_{HD} = -1$ transition in HD for the same initial state on the two PESs.

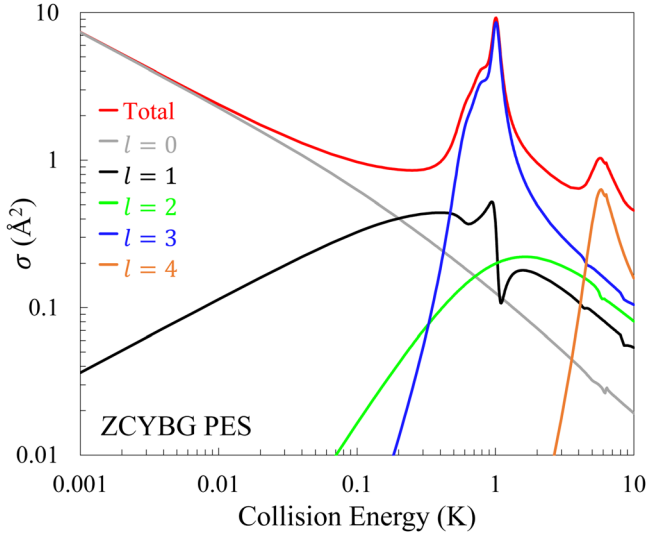

Fig. 6 Partial-wave resolved cross sections for the $j_{HD} = 2 \rightarrow j'_{HD} = 0$ rotational transition in HD(v_{HD} = 1) on the ZCYBG PES as function of the collision energy. The red curve denotes the total quenching cross section while grey, black, green, blue, and orange curves show contributions from l = 0, 1, 2, 3, and 4 respectively. It can be seen that the primary peak is due to l = 3 while the secondary peak arises mainly from l = 4.

Results correspond to elastically scattered D_2, *i.e.*, $j_{D_2} = j'_{D_2} = 0$. For this case, the quenching cross section is an order of magnitude larger than the $\Delta j_{HD} = -2$ transition, as it is driven by the leading anisotropic term of the interaction potential depicted in Fig. 1. Similar to the $\Delta j_{HD} = -2$ transition, the primary resonance peak is observed at 1.02 and 0.62 K, respectively, on the ZCYBG and Hinde PESs. A partial wave analysis reveals that the same partial waves are responsible for the resonances in both $\Delta j_{HD} = -1$ and $\Delta j_{HD} = -2$ transitions. For $\Delta j_{HD} = -1$, the $l = 3$ resonance originates from $J = 2$, 5 (shoulder region) and $J = 3$, 4 (main peak). The secondary resonance peak is also observed at the same energy as the $j_{HD} = 2 \rightarrow j'_{HD} = 0$ transition, and the Hinde PES predicts slightly larger cross sections compared to the ZCYBG PES (less than 2 Å^2).

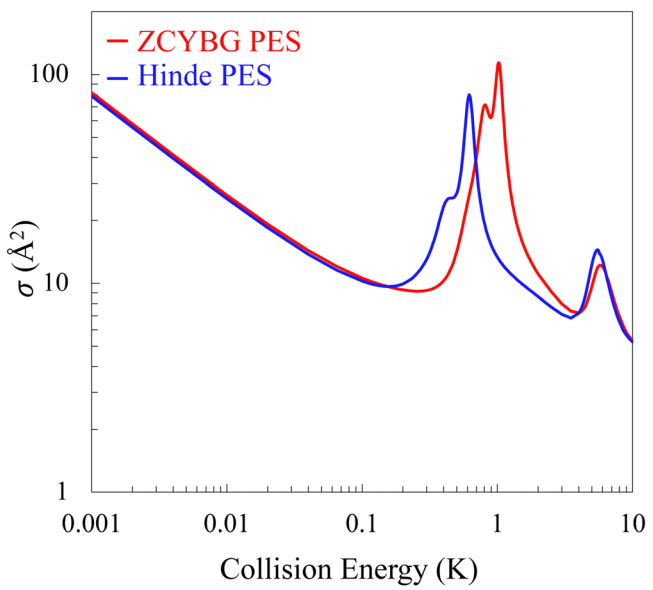

Fig. 7 Collision energy dependence of the inelastic cross section for $\Delta j_{HD} = -1$ transition in HD(v_{HD} = 1). The blue and red curves represent results obtained on the Hinde and ZCYBG PESs, respectively.

3.3 Effect of *ortho* and *para*-D_2 colliders

The experiments of Perreault *et al.*[53,54] employed *n*-D_2 collision partner with populations of 59% in j = 0, 33% in j = 1 and 8% in j = 2, all in the v = 0 vibrational level. Results presented in Fig. 5–7 correspond to $D_2(j_{D_2} = 0)$. Cross sections for $D_2(j_{D_2} = 1)$ collisions are shown in Fig. 8 for both Hinde and ZCYBG PESs. The dominant peaks on both PESs arise from $l = 1$ and $l' = 3$ partial waves while the secondary peaks correspond to $l = 3$, $l' = 3$, 5 though the $l' = 5$ feature is absent for the Hinde PES. The resonance positions predicted by the two potentials are somewhat different for the two low-energy resonances illustrating the sensitivity of the resonance features to the attractive part of the two PESs. However, both potentials predict the same position and similar magnitudes for the resonance near 6 K. The primary peak in the cross section is an $l = 1 \rightarrow l' = 3$ resonance, which is more prominent on the ZCYBG PES, occurring at about 0.15 K compared to about 1 K for the Hinde PES. This could be attributed to the small differences in the well-depth of the isotropic potential as shown in Fig. 1. This applies to both $\Delta j_{HD} = -2$ and $\Delta j_{HD} = -1$ transitions shown in Fig. 8. Compared to *ortho*-$D_2(j_{D_2} = 0)$ collider, for which the dominant resonance was found for $l = 3$, for *para*-$D_2(j_{D_2} = 1)$ both $l = 1$ and $l = 3$ contribute to the resonance features.

In the low-energy limit, both *ortho* and *para*-D_2 are dominated by *s*-wave scattering, and the cross sections are nearly identical for the ZCYBG and Hinde PESs. While low-energy scattering is generally very sensitive to the fine details of the interaction potential, the fact that the cross sections are identical on the two PESs, implies that the long-range part of the two PESs is accurately described. We also note that in the scattering calculations, we use the same diatomic potential energy function for HD and D_2 molecules, the H_2 potential of Schwenke.[90]

3.4 Energy transfer from HD to D_2

In their analysis of the experiments, Perreault *et al.*[53,54] treated the D_2 collision partner as a spectator, *i.e.*, its rotational level is considered to be unchanged during the collision. Because the rotational constant of D_2 ($\sim$43 K for v = 0) is significantly smaller than that of HD ($\sim$64 K for v = 0 and $\sim$61 K for v = 1) this assumption may not be valid as a $\Delta j_{HD} = -2$ transition in HD can accompany a $\Delta j_{D_2} = +2$ transition in D_2. Indeed, the energy difference of j = 0 and j = 2 state of the HD molecule in v = 1 is about $\sim$367 K, while the same for $D_2(v = 0)$ is about $\sim$258 K. Therefore, the energy released from quenching of HD in a $j_{HD} = 2 \rightarrow j'_{HD} = 0$ transition is sufficient to excite *ortho*-D_2 molecule from $j_{D_2} = 0 \rightarrow j'_{D_2} = 2$. This energy transfer is only possible for the *ortho*-D_2 collision partner in $j_{D_2} = 0$ because the released energy from the quenching of HD is not sufficient to

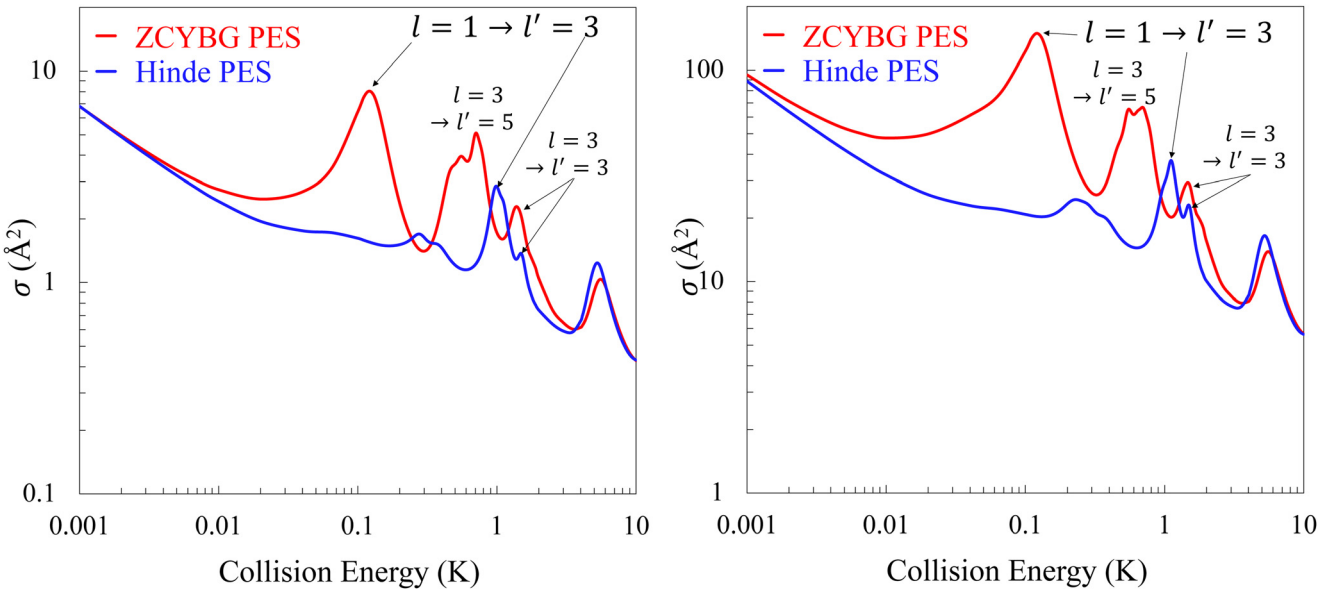

Fig. 8 Integral cross sections for $\Delta j_{HD} = -2$ (left panel) and $\Delta j_{HD} = -1$ (right panel) transitions in HD by collision with *para*-$D_2(j_{D_2} = 1)$. The red and blue curves represent results obtained on the ZCYBG and Hinde PESs, respectively. An $l = 1 \rightarrow l' = 3$ resonance is seen to be more prominent as compared to the $l = 3$ resonance for *ortho*-D_2.

excite *para*-D_2 molecule from $j_{D_2} = 1 \rightarrow j'_{D_2} = 3$ state. Also, the energy released from HD quenching from $j_{HD} = 2 \rightarrow j'_{HD} = 1$ transition in $v = 1$ is about $\sim$245 K, and thus, not sufficient to excite the *ortho*-D_2 molecule from $j_{D_2} = 0 \rightarrow j'_{D_2} = 2$. Therefore, an accurate characterization of the experimental results of Perreault *et al.*[53] must include concurrent excitation of D_2 from $j_{D_2} = 0 \rightarrow j'_{D_2} = 2$ in the quenching of HD from $j_{HD} = 2 \rightarrow j'_{HD} = 0$.

We investigated this process of energy exchange between HD and D_2, and the resulting cross section is shown in Fig. 9 as a function of the collision energy. The results show that this process has a cross section that is a factor of 4 greater than pure rotational quenching of HD from $j_{HD} = 2 \rightarrow j'_{HD} = 0$ without D_2 rotational excitation. Except for the resonance peaks both PESs predict similar results. A partial wave analysis reveals that the resonance peaks arise from the same partial waves as in elastically scattered D_2 ($\Delta j_{D_2} = 0$).

Results in Fig. 9 illustrate that the energy exchange process between HD and D_2 cannot be ignored in the $j_{HD} = 2 \rightarrow j'_{HD} = 0$ rotational quenching of the HD molecule in HD($v_{HD} = 1, j_{HD} = 2$) + $D_2(j_{D_2} = 0)$ collisions. As such, this transition is more important, and should be considered together with other transitions in characterizing the experimental data. However, this process was not included in the original analysis of the experimental data,[54] presumably due to lack of information on the cross section for this process. Instead, the experimental studies explained their results using a partner reorientation theory that accounts for m' changing collisions of the *para*-$D_2(j_{D_2} = 1)$ partner. While such collisions may indeed occur in the scattering experiment, and the experimental data may well be reproduced by a model including this effect, a correct description should also account for rotational excitation of D_2 in $j_{D_2} = 0$ collisions. As mentioned above the cross sections for $j_{HD} = 2 \rightarrow j'_{HD} = 0$ transitions in HD($v_{HD} = 1$) by *para* and *ortho*-D_2 have similar magnitude for elastically scattered D_2, but the energy exchange process between HD and D_2 yields cross sections that are four times larger,

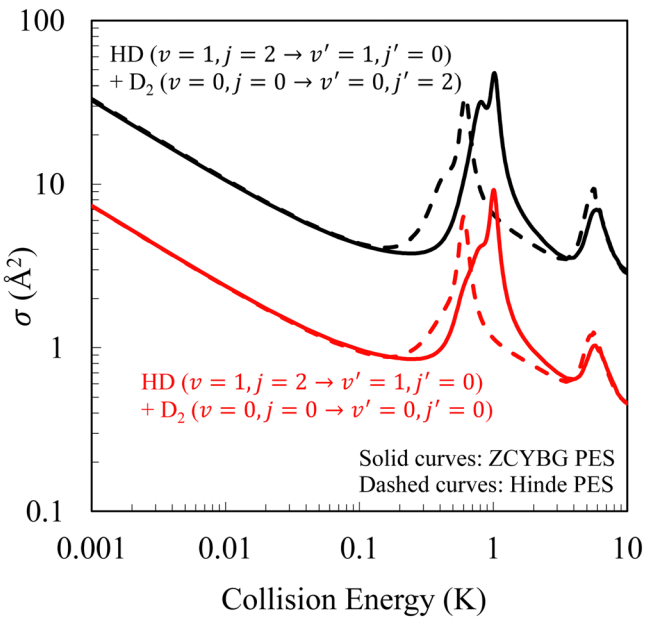

Fig. 9 Integral cross sections as function of the collision energy for rotational quenching of HD from from $j_{HD} = 2 \rightarrow j'_{HD} = 0$ with and without rotational excitation of the D_2 molecule from $j_{D_2} = 0$ to $j'_{D_2} = 2$. The red curves represent the elastic transition in D_2 ($\Delta j_{D_2} = 0$) (cross sections depicted in Fig. 5) while the black curves denote the D_2 rotational excitation channel. The solid and dashed curves show results computed on the ZCYBG and Hinde PES, respectively.

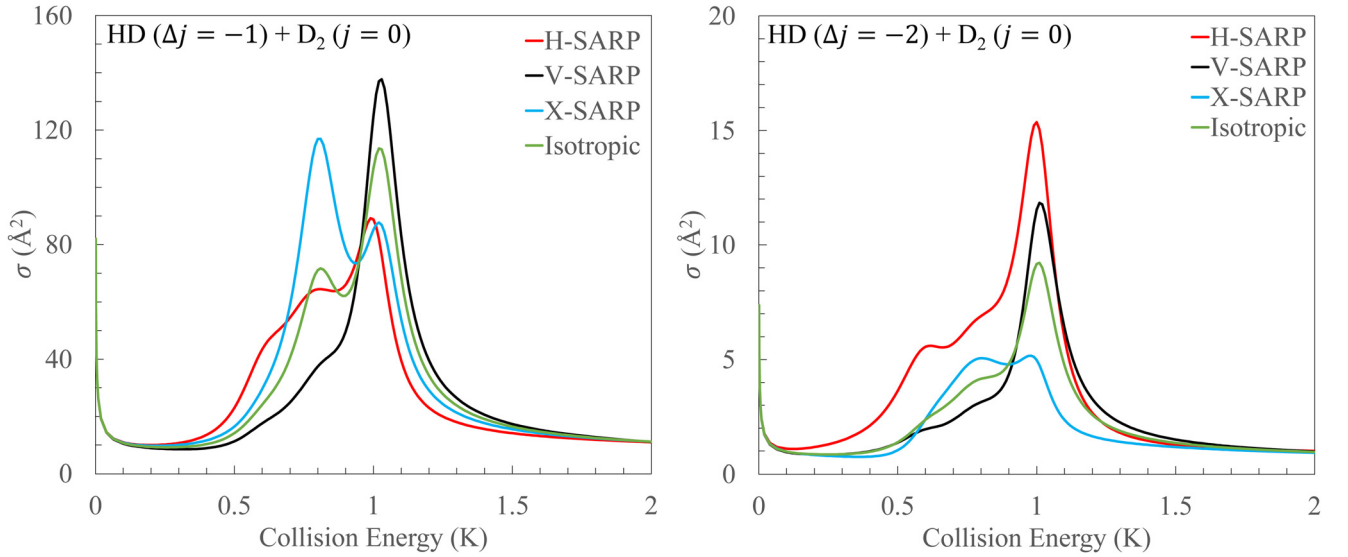

Fig. 10 Integral cross sections as a function of the collision energy for the $v_{HD} = 1, j_{HD} = 2 \rightarrow v'_{HD} = 1, j'_{HD} = 1$ ($\Delta j_{HD} = -1$) (left panel) and $v_{HD} = 1, j_{HD} = 2 \rightarrow v'_{HD} = 1, j'_{HD} = 0$ ($\Delta j_{HD} = -2$) transitions (right panel) in collision with $D_2(j_{D_2} = 0)$. Green, red, blue, and black colors represent the isotropic, H-SARP, X-SARP, and V-SARP cross sections, respectively.

making it an important mechanism in interpreting the experimental data. This is further supported by the comparisons with the results of Buck *et al.* shown in Fig. 3. Among the various transitions reported in Fig. 3, we would like to draw attention to the 02 → 20 transition. This is the reverse process in which HD is excited from $j_{HD} = 0 \rightarrow j'_{HD} = 2$ while D_2 relaxes from $j_{D_2} = 2 \rightarrow j'_{D_2} = 0$. The agreement between the two calculations is excellent over the entire range of the scattering angle for both collision energies reported in Fig. 3. This further validates the importance of the D_2 rotational excitation process in the $\Delta j_{HD} = -2$ quenching of the HD molecule. We note that the cross sections for HD($v = 1, j = 2 \rightarrow v' = 1, j' = 0$) + D_2($v = 0, j = 0 \rightarrow v' = 0, j' = 2$) and its reverse process are connected by the principle of microscopic reversibility.

The ICSs for the different processes discussed thus far correspond to isotropic preparations of the collision partners. The various SARP prepared ICSs are compared against their isotropic counterpart in Fig. 10 for $\Delta j_{HD} = -1$ (left panel) and $\Delta j_{HD} = -2$ (right panel) in HD($v_{HD} = 1, j_{HD} = 2$) + $D_2(j_{D_2} = 0)$ collisions. It is seen that the cross sections are strongly sensitive to the SARP preparation, in particular, in the vicinity of the resonance. The X-SARP preparation corresponds to $\beta = \pm 45^\circ$ and refers to a bi-axial state that involves linear combinations of $m_{j_{HD}} = \pm 1$ states.[64] For the $\Delta j_{HD} = -1$ transition the V-SARP preparation maximizes the cross section at the resonance peak near 1 K while for the $\Delta j_{HD} = -2$ transition it is the H-SARP preparation that maximizes the cross section. For $\Delta j_{HD} = -2$, the X-SARP preparation leads to the smallest ICS. However, for the $\Delta j_{HD} = -1$ transition, the less prominent shoulder peak on the left of the main peak near 1 K becomes even more prominent for the X-SARP preparation and becomes comparable in magnitude to the main peak of the isotropic case. Thus, strong stereodynamic effect is seen in the resonance region that allows considerable control of the ICS through alignment of the HD rotational angular momentum.

3.5 Comparisons with SARP experiments

3.5.1 $\Delta j = -1$ rotational transition in HD. The main goal of this work is to compare our theoretical predictions with the experimental results of Perreault *et al.* for the H-SARP and V-SARP preparations of the HD molecule in the $v_{HD} = 1, j_{HD} = 2$ initial state.[53,54] The experimental results are not energy resolved but averaged over the relative velocities of HD and D_2 present in the experiment. This can be done using the velocity distributions of the HD and D_2 molecules in the molecular beam as discussed by Perreault *et al.*[53,54] and in our prior work.[68] The HD and D_2 velocity distributions from the experiments are given by a Gaussian distribution P, where $P(v_{HD}) \propto f(u_{HD} = 2015, \sigma_{HD}{}^2 = 173^2/2)$ and $P(v_{D_2}) \propto f(u_{D_2} = 2061, \sigma_{D_2}{}^2 = 132^2/2)$ for HD and D_2 respectively, where v, u, and σ are expressed in units of m s^{-1}.[53] The relative velocity is given by $v_r{}^2 = v_{HD}{}^2 + v_{D_2}{}^2 - 2v_{HD}v_{D_2}\cos\chi$, where χ is the crossing angle between the two beams of HD and D_2. A beam divergence of 12 mrad in the transverse direction has been reported by Perreault *et al.*[54] In the analysis of the experimental data by Perreault *et al.*[53,54] a simpler 1-dimensional (1D) relative velocity distribution corresponding to $\chi = 0$ is used. A 3D relative velocity distribution obtained from a Monte-Carlo sampling of χ consistent with the reported beam divergence is used in our analysis. However, we have verified that a 1D velocity distribution yields nearly identical results.

In constructing the velocity averaged differential rate, the *ortho* and *para*-D_2 contributions are weighted by their populations of 59% and 33%, respectively for $j = 0$ and 1. There is a minor 8% contribution from $j = 2$ but it is neglected in our calculations. While we have computed the DCS on both PESs,

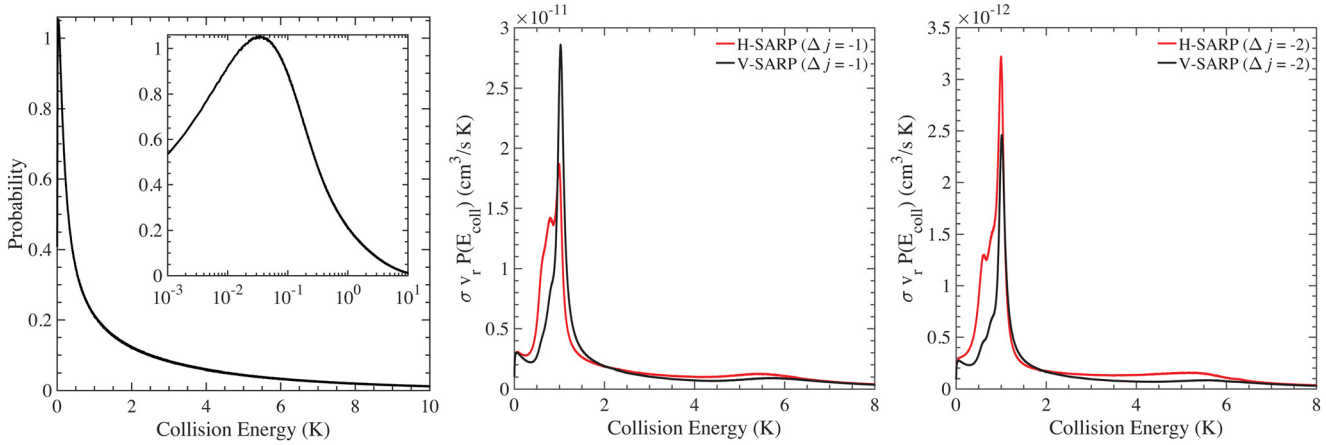

Fig. 11 The normalized collision energy distribution with the inset showing a magnified view in the 0.001–1 K range in logarithm scale (left panel). The middle and the right panels show, respectively, the product of the cross section, relative velocity and the energy distribution as a function of the collision energy for H-SARP (red curves) and V-SARP (black curves) preparations of the HD molecule. Results for $\Delta j_{HD} = -1$ are shown in the middle panel while that for $\Delta j_{HD} = -2$ are shown on the right panel. For both transitions, the collision partner is $D_2(j_{D_2} = 0)$ and it is scattered elastically. Please note the different vertical scale between the middle and right panels.

we present the results from the ZCYBG PES in the main text, and provide that of the Hinde PES in the ESI.†

The collision energy distribution evaluated from the 3D relative velocity distribution is shown in the left panel of Fig. 11. In the middle and the right panel of Fig. 11, we show ICS for H-SARP and V-SARP preparations multiplied by the relative velocity and the corresponding energy distribution as a function of the collision energy in Kelvin for $\Delta j_{HD} = -1$ and -2, respectively. For both cases, the collision partner is $D_2(j = 0)$ and the $\Delta j_{HD} = -2$ process does not include contributions from rotational excitation of the D_2 molecule. As can be seen, for both H-SARP and V-SARP preparations, the energy dependent rate coefficients convoluted with the energy distribution peak near 1 K, and are dominated by contributions from the $l = 3$ partial wave resonance. We note that the analysis of the experimental data is limited to $l = 0$ and $l = 1$ and that the experimental results are not energy resolved.[53,54] Thus, the energy dependent rate coefficient weighted with the collision energy distribution presented here can provide key insights into specific partial wave resonances that contribute to the measured angular distribution.

Fig. 12 shows a comparison of the experimental angular distribution of Perreault *et al.*[53] and our theoretical results for the $j_{HD} = 2 \rightarrow j'_{HD} = 1$ transition in $HD(v_{HD} = 1, \Delta j_{HD} = -1)$. The left panel shows the results for the H-SARP preparation while the right panel shows that for the V-SARP case. We note that the experimental data are reported in arbitrary units and they do not correspond to absolute cross sections (rates). Thus, to enable comparison with experiments, the experimental results are scaled appropriately. The comparison is overall good for both H-SARP and V-SARP preparations. However, the peaks in the experimental and theory results are

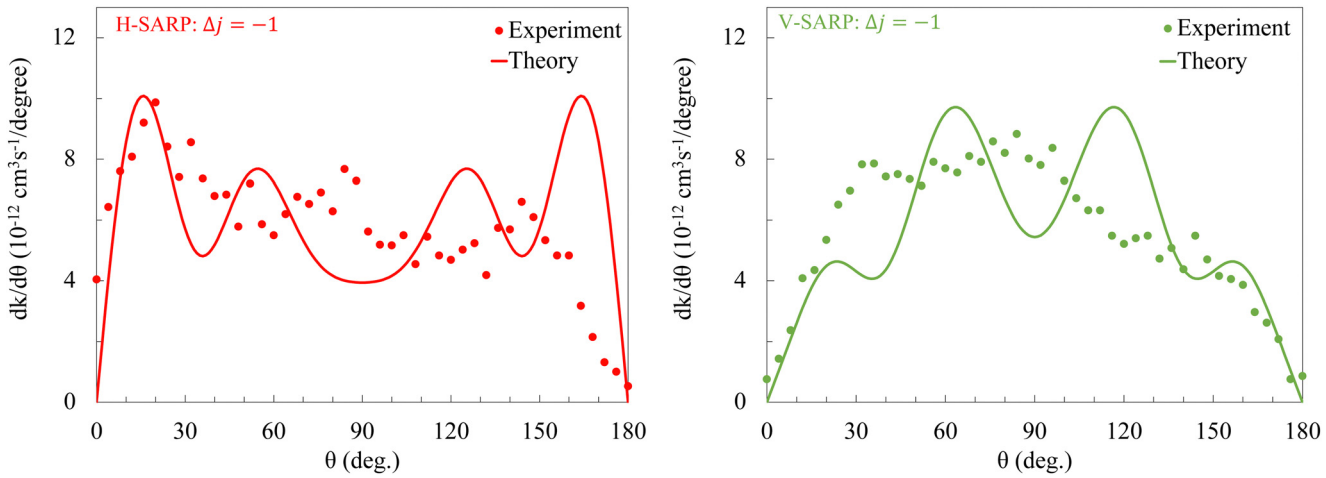

Fig. 12 A comparison between experiment and theory of the differential rate coefficients averaged over the relative energy distribution for rotational quenching of HD for $j_{HD} = 2 \rightarrow j'_{HD} = 1$ transition. The left and right panels correspond to H-SARP and V-SARP preparations, respectively. The experimental data by Perreault *et al.*[53] are shown by filled circles while the theoretical results are shown by solid and dashed curves.

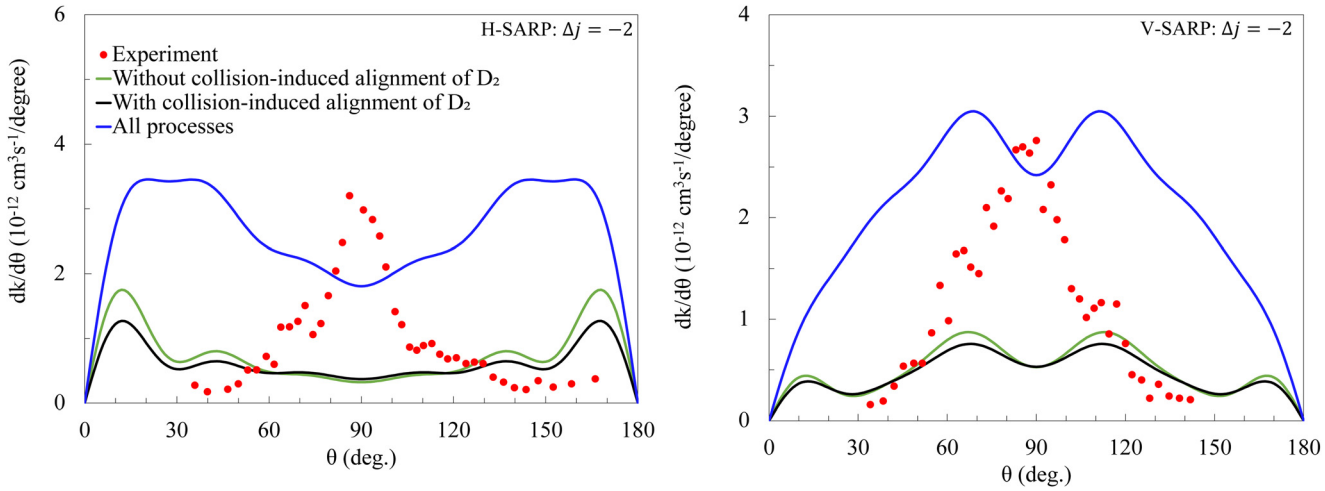

Fig. 13 Differential rates in H-SARP and V-SARP for $j_{HD} = 2 \rightarrow j'_{HD} = 0$ rotational transition in HD induced by collisions with D_2. H-SARP (left panel) and V-SARP (right panel) results from Perreault *et al.*[54] (red dots) are compared against theoretical results (solid curves) from this work using the ZCYBG PES. Black and green curves represent, respectively, results with and without considering collision-induced alignment of D_2 in $D_2(j = 1)$ collisions, while blue curve includes this process and the D_2 excitation from $j = 0 \rightarrow j' = 2$.

largely out-of-phase except for the forward scattering peak in the H-SARP result.

3.5.2 $\Delta j = -2$ rotational transition in HD. Finally, we present the angular dependence of the H-SARP and V-SARP differential rates for the $j_{HD} = 2 \rightarrow j'_{HD} = 0$ rotational transition in HD($v_{HD} = 1$).[54] Fig. 13 provides a comparison between experiment and theory with filled circles representing the experimental results and solid curves denoting theoretical results. For this case, Perreault *et al.*[54] have proposed a partner re-orientation theory that involves m_j changing collisions of the $D_2(j = 1)$ partner to account for the experimental findings (strictly speaking, we believe "partner re-orientation" is a misleading terminology because the D_2 molecule is unprepared initially and its angular momentum is not polarized. We believe, "collision-induced alignment" is a more appropriate terminology and we adopt in our discussions here). Specifically, the H-SARP angular distribution could not be reproduced by their non-linear fitting scheme when m_j changing collisions of $D_2(j = 1)$ are not considered.[54] Thus, three different scenarios have been examined from a theoretical standpoint: (i) m_j changing collisions of $D_2(j = 1)$ is not invoked (shown by the green curve); (ii) m_j changing collisions of $D_2(j = 1)$ are considered with the corresponding results shown by the black curve. In both these cases, we have omitted contributions from the rotational excitation channel in $D_2(j = 0)$ collisions, *i.e.*, only direct relaxation of HD is considered. Both yield comparable results and display strong deviation from the experiment for H-SARP and V-SARP preparations. Lastly, (iii) we include the D_2 rotational excitation channel in $D_2(j = 0)$ collisions as well as collision-induced alignment of the $D_2(j = 1)$ partner. Note that the D_2 rotational excitation channel has the largest cross section as shown in Fig. 9. Despite including all possible processes the agreement between theory and experiment is not significantly improved, although the V-SARP results depict a broad central peak consistent with sideways scattering. The experimental data display very similar features for both H-SARP and V-SARP preparations, which is very different from the $j_{HD} = 2 \rightarrow j'_{HD} = 1$ transition. In general, for H-SARP collisions, two dominant peaks are observed at forward and backward scattering angles with a less prominent peak at 90 degrees. This appears to be the case for all of the atom–molecule and molecule–molecule collisions for which SARP experiments have been reported so far.[55–58,60–62] A strong central peak is typical for the V-SARP case. Such features are also implied by the values of the reduced rotation matrix elements that characterize these preparations (*e.g.*, see Fig. 2 of ref. 67). It is unlikely that the lack of agreement with experiment for this case is due to the PES employed as corresponding results on the Hinde PES presented in the ESI† also depict similar comparisons. At this point we can only speculate on the source of the discrepancy but energy-resolved measurements may yield more insight.

Perreault *et al.*[54] have discussed the possibility of including the D_2 rotational excitation channel in their analysis of the experimental data. However, they excluded this process in favor of m_j changing collisions of $D_2(j = 1)$ as the measured time-of-flight spectrum of the scattered HD molecules appeared to be consistent with this mechanism. The D_2 rotational excitation channel would require lower HD speeds based on energy conservation but this seems to be not supported by the time-of-flight data. Beam-divergence is not considered in the experiments and it is not clear whether this would have an impact on the measured time-of-flight spectrum. We would like to point out that angular momentum conservation effects would produce similar outgoing partial waves regardless of whether the D_2 rotational excitation process or m_j changing collisions of the $D_2(j = 1)$ partner is invoked in fitting the experimental data. In our prior simulations of HD($v = 1, j = 2$) + H_2 collisions where $j_{HD} = 2 \rightarrow j'_{HD} = 0$ collisions were probed by the SARP

techniques[54] excellent agreement with experiment is observed without invoking m_j changing collisions of the $H_2(j = 1)$ partner.[68] In this case, rotational excitation of $H_2(j = 0)$ is not energetically possible at the collision energies involved in the experiment. Similarly, we have obtained excellent agreement with the SARP experiments for aligned collisions of two $D_2(v = 2, j = 2)$ molecules using the ZCYBG PES adopted in this study.[43,71] Indeed, in this case it was important to include the effect of four-vector correlations in the theoretical formalism as well as collisions involving aligned $D_2(v = 2, j = 2)$ and unpolarized $D_2(v = 0, j = 1, 2)$ molecules present in the beam in reproducing key features of the measured H-SARP angular distribution. Thus, all relevant processes should be taken into account in the analysis of the experimental data as done in this work for HD + D_2.

4 Conclusions

In this paper, we report theoretical studies of the stereodynamics and quantum-controlled scattering of HD and D_2 for the first time. It is found that the dominant inelastic channel in the rotational quenching of HD from $v_{HD} = 1, j_{HD} = 2 \rightarrow v'_{HD} = 1, j'_{HD} = 0$ involves an energy transfer to D_2 leading to $j_{D_2} = 0 \rightarrow j'_{D_2} = 2$ rotational excitation of the D_2 molecule. This transition conserves the total molecular rotational angular momentum and has a cross section that is 4 times larger than that of direct relaxation of HD without D_2 rotational excitation. A partial wave analysis shows a dominant $l = 3$ resonance for both $\Delta j_{HD} = -2$ and $\Delta j_{HD} = -1$ transition in HD for *ortho*-$D_2(j = 0)$, while both $l = 1$ and $l = 3$ resonances contribute to *para*-$D_2(j = 1)$ collisions. These results are found to be largely insensitive to the choice of the potential energy surfaces for the H_2–H_2 system adopted in the scattering calculations. Our computed results are in excellent agreement with prior calculations and measurements of differential cross sections for elastic and rotationally inelastic collisions of HD and D_2 at higher collision energies. However, the agreement is less satisfactory with recent SARP experiments that report stereodynamic control of rotational quenching in $HD(v_{HD} = 1, j_{HD} = 2)$ + D_2 collisions. While our results generally agree with experiments for the $j_{HD} = 2 \rightarrow j'_{HD} = 1$ transition, a significant discrepancy is observed for the $j_{HD} = 2 \rightarrow j'_{HD} = 0$ transition in HD. The discrepancy persists regardless of whether D_2 rotational excitation channel is considered in the theoretical simulations. We believe, a re-analysis of the experimental data including the D_2 rotational excitation channel in $D_2(j = 0)$ collisions or measurements of energy resolved cross sections may help resolve the discrepancy.

Author contributions

Quantum scattering calculations were primarily carried out by B. M. with assistance from N. B. and J. F. E. C. All authors contributed to data analysis, manuscript preparation, and editing.

Conflicts of interest

There are no conflicts to declare.

Acknowledgements

We thank Dick Zare, Nandini Mukherjee, William Perreault, and Haowen Zhou for many stimulating discussions and sharing their experimental data. This work is supported in part by NSF grant No. PHY-2110227 (N. B.) and by a DoD MURI grant from Army Research Office (Grant No. W911NF-19-1-0283 to H. G. and N. B.). F. J. A. acknowledges funding by the Spanish Ministry of Science and Innovation (grant PID2021-122839NB-I00). P. G. J. acknowledges Grant No. PID2020-113147GA-I00 funded by MCIN/AEI/10.13039/501100011033 (Spanish Ministry of Science and Innovation). J. F. E. C. acknowledges support from the U.K. Engineering and Physical Sciences Research Council (EPSRC) Grant No. EP/W00299X/1.

Notes and references

1 P. C. Stancil, S. Lepp and A. Dalgarno, *Astrophys. J.*, 1998, **509**, 1.
2 S. C. O. Glover and T. Abel, *Mon. Not. R. Astron. Soc.*, 2008, **388**, 1627–1651.
3 D. Galli and F. Palla, *Astron. Astrophys.*, 1998, **335**, 403.
4 Y. Wan, N. Balakrishnan, B. H. Yang, R. C. Forrey and P. C. Stancil, *Mon. Not. R. Astron. Soc.*, 2019, **488**, 381.
5 N. Balakrishnan, J. F. E. Croft, B. H. Yang, R. C. Forrey and P. C. Stancil, *Astrophys. J.*, 2018, **866**, 95.
6 D. Puy, G. Alecian, J. L. Bourlot, J. Leorat and G. D. Forets, *Astron. Astrophys.*, 1993, **267**, 337.
7 D. Galli and F. Palla, *Planet. Space Sci.*, 2002, **50**, 1197.
8 S. Lacour, M. K. André, P. Sonnentrucker, F. L. Petit, D. E. Welty, J. M. Desert, R. Ferlet, E. Roueff and D. G. York, *Astron. Astrophys.*, 2005, **430**, 967.
9 H. S. Liszt, *Astrophys. J.*, 2015, **799**, 66.
10 I. D. McGreer and G. L. Bryan, *Astrophys. J.*, 2008, **685**, 8.
11 S. Hirano, T. Hosokawa, N. Yoshida, K. Omukai and H. W. Yorke, *Mon. Not. R. Astron. Soc.*, 2015, **448**, 568.
12 E. Ripamonti, *Mon. Not. R. Astron. Soc.*, 2007, **376**, 709.
13 Y. Wan, B. H. Yang, P. C. Stancil, N. Balakrishnan, N. J. Parekh and R. C. Forrey, *Astrophys. J.*, 2018, **862**, 132.
14 C. Joblin, E. Bron, C. Pinto, P. Pilleri, F. L. Petit, M. Gerin, J. L. Bourlot, A. Fuente, O. Berne and J. R. Goicoechea, *et al.*, *Astron. Astrophys.*, 2018, **615**, A129.
15 E. A. Bergin, L. I. Cleeves, U. Gorti, K. Zhang, G. A. Blake, J. D. Green, S. M. Andrews, N. J. Evans II, T. Henning and K. Öberg, *et al.*, *Nature*, 2013, **493**, 644.
16 C. M. Wright, E. F. V. Dishoeck, P. Cox, S. D. Sidher and M. F. Kessler, *Astrophys. J.*, 1999, **515**, L29.
17 E. T. Polehampton, J. P. Baluteau, C. Ceccarelli, B. M. Swinyard and E. Caux, *Astron. Astrophys.*, 2002, **388**, L44.
18 H. Kamaya and J. Silk, *Mon. Not. R. Astron. Soc.*, 2003, **339**, 1256.

19 D. A. Neufeld, J. D. Green, D. J. Hollenbach, P. Sonnentrucker, G. J. Melnick, E. A. Bergin, R. L. Snell, W. J. Forrest, D. M. Watson and M. J. Kaufman, *Astrophys. J.*, 2006, **647**, L33.
20 D. Flower, *Molecular collisions in the interstellar medium*, Cambridge University Press, 2007, vol. 42.
21 D. R. Flower, *Mon. Not. R. Astron. Soc.*, 2000, **318**, 875.
22 R. J. Hinde, *J. Chem. Phys.*, 2008, **128**, 154308.
23 J. Zuo, J. F. E. Croft, Q. Yao, N. Balakrishnan and H. Guo, *J. Chem. Theory Comput.*, 2021, **17**, 6747.
24 G. Garberoglio, P. Jankowski, K. Szalewicz and A. H. Harvey, *J. Chem. Phys.*, 2012, **137**, 154308.
25 S. F. dos Santos, N. Balakrishnan, S. Lepp, G. Quéméner, R. C. Forrey, R. J. Hinde and P. C. Stancil, *J. Chem. Phys.*, 2011, **134**, 214303.
26 Y. Liu, P. G. Jambrina, J. F. E. Croft, N. Balakrishnan, F. J. Aoiz and H. Guo, *J. Chem. Theory Comput.*, 2024, 1829.
27 J. L. Bohn, A. M. Rey and J. Ye, *Science*, 2017, **357**, 1002.
28 V. V. Albert, J. P. Covey and J. Preskill, *Phys. Rev. X*, 2020, **10**, 31050.
29 J. Toscano, H. J. Lewandowski and B. R. Heazlewood, *Phys. Chem. Chem. Phys.*, 2020, **22**, 9180.
30 M. G. Hu, Y. Liu, M. A. Nichols, L. Zhu, G. Quéméner, O. Dulieu and K. K. Ni, *Nat. Chem.*, 2021, **13**, 435.
31 P. G. Jambrina, J. F. E. Croft, N. Balakrishnan and F. J. Aoiz, *Phys. Chem. Chem. Phys.*, 2021, **23**, 19364.
32 B. K. Kendrick, H. Li, M. Li, S. Kotochigova, J. F. E. Croft and N. Balakrishnan, *Phys. Chem. Chem. Phys.*, 2021, **23**, 5096.
33 Y. Segev, M. Pitzer, M. Karpov, N. Akerman, J. Narevicius and E. Narevicius, *Nature*, 2019, **572**, 189.
34 H. Son, J. J. Park, W. Ketterle and A. O. Jamison, *Nature*, 2020, **580**, 197.
35 L. Anderegg, L. W. Cheuk, Y. Bao, S. Burchesky, W. Ketterle, K. K. Ni and J. M. Doyle, *Science*, 2019, **365**, 1156.
36 Y. Liu and K. K. Ni, *Annu. Rev. Phys. Chem.*, 2022, **73**, 73.
37 R. V. Krems, *Phys. Chem. Chem. Phys.*, 2008, **10**, 4079.
38 L. D. Carr, D. DeMille, R. V. Krems and J. Ye, *New J. Phys.*, 2009, **11**, 55049.
39 B. K. Stuhl, M. T. Hummon and J. Ye, *Annu. Rev. Phys. Chem.*, 2014, **65**, 501.
40 Y. Liu, M. G. Hu, M. A. Nichols, D. Yang, D. Xie, H. Guo and K. K. Ni, *Nature*, 2021, **593**, 379.
41 N. Balakrishnan, *J. Chem. Phys.*, 2016, **145**, 150901.
42 B. R. Heazlewood and T. P. Softley, *Nat. Rev. Chem.*, 2021, **5**, 125.
43 J. F. E. Croft, P. G. Jambrina, F. J. Aoiz, H. Guo and N. Balakrishnan, *J. Phys. Chem. A*, 2023, **127**, 1619.
44 J. A. Blackmore, L. Caldwell, P. D. Gregory, E. M. Bridge, R. Sawant, J. Aldegunde, J. M. Petit, D. Jaksch, J. M. Hutson and B. E. Sauer, *et al.*, *Quantum Sci. Technol.*, 2018, **4**, 14010.
45 L. W. Cheuk, L. Anderegg, Y. Bao, S. Burchesky, S. Y. Scarlett, W. Ketterle, K. K. Ni and J. M. Doyle, *Phys. Rev. Lett.*, 2020, **125**, 43401.
46 P. Aggarwal, Y. Yin, K. Esajas, H. L. Bethlem, A. Boeschoten, A. Borschevsky, S. Hoekstra, K. Jungmann, V. R. Marshall and T. B. Meijknecht, *et al.*, *Phys. Rev. Lett.*, 2021, **127**, 173201.
47 S. Jurgilas, A. Chakraborty, C. J. H. Rich, L. Caldwell, H. J. Williams, N. J. Fitch, B. E. Sauer, M. D. Frye, J. M. Hutson and M. R. Tarbutt, *Phys. Rev. Lett.*, 2021, **126**, 153401.
48 L. Anderegg, B. L. Augenbraun, Y. Bao, S. Burchesky, L. W. Cheuk, W. Ketterle and J. M. Doyle, *Nat. Phys.*, 2018, **14**, 890.
49 J. F. E. Croft, J. L. Bohn and G. Quéméner, *Phys. Rev. A*, 2020, **102**, 33306.
50 D. Yang, J. Huang, X. Hu, D. Xie and H. Guo, *J. Chem. Phys.*, 2020, **152**, 241103.
51 N. Mukherjee and R. N. Zare, *J. Chem. Phys.*, 2011, **135**, 024201.
52 N. Mukherjee, W. E. Perreault and R. N. Zare, *J. Phys. B: At., Mol. Opt. Phys.*, 2017, **50**, 144005.
53 W. E. Perreault, N. Mukherjee and R. N. Zare, *Science*, 2017, **358**, 356.
54 W. E. Perreault, N. Mukherjee and R. N. Zare, *Nat. Chem.*, 2018, **10**, 561.
55 H. Zhou, W. E. Perreault, N. Mukherjee and R. N. Zare, *J. Chem. Phys.*, 2021, **154**, 104309.
56 W. E. Perreault, H. Zhou, N. Mukherjee and R. N. Zare, *J. Chem. Phys.*, 2022, **157**, 144301.
57 H. Zhou, W. E. Perreault, N. Mukherjee and R. N. Zare, *Science*, 2021, **374**, 960.
58 W. E. Perreault, H. Zhou, N. Mukherjee and R. N. Zare, *J. Phys. Chem. Lett.*, 2022, **13**, 10912.
59 W. E. Perreault, N. Mukherjee and R. N. Zare, *J. Chem. Phys.*, 2016, **145**, 154203.
60 W. E. Perreault, N. Mukherjee and R. N. Zare, *J. Chem. Phys.*, 2019, **150**, 174301.
61 H. Zhou, W. E. Perreault, N. Mukherjee and R. N. Zare, *Nat. Chem.*, 2022, **14**, 658.
62 W. E. Perreault, H. Zhou, N. Mukherjee and R. N. Zare, *Phys. Rev. Lett.*, 2020, **124**, 163202.
63 W. E. Perreault, N. Mukherjee and R. N. Zare, *Chem. Phys.*, 2018, **514**, 150.
64 N. Mukherjee, *J. Phys. Chem. A*, 2023, **127**, 418.
65 N. Balakrishnan, P. G. Jambrina, J. F. E. Croft, H. Guo and F. J. Aoiz, *Chem. Commun.*, 2024, **60**, 1239.
66 Y. Wang, J. Huang, W. Wang, T. Du, Y. Xie, Y. Ma, C. Xiao, Z. Zhang, D. H. Zhang and X. Yang, *Science*, 2023, **379**, 191.
67 J. F. E. Croft and N. Balakrishnan, *J. Chem. Phys.*, 2019, **150**, 164302.
68 J. F. E. Croft, N. Balakrishnan, M. Huang and H. Guo, *Phys. Rev. Lett.*, 2018, **121**, 113401.
69 M. Morita and N. Balakrishnan, *J. Chem. Phys.*, 2020, **153**, 184307.
70 M. Morita and N. Balakrishnan, *J. Chem. Phys.*, 2020, **153**, 091101.
71 P. G. Jambrina, J. F. E. Croft, J. Zuo, H. Guo, N. Balakrishnan and F. J. Aoiz, *Phys. Rev. Lett.*, 2023, **130**, 33002.
72 P. G. Jambrina, M. Morita, J. F. E. Croft, F. J. Aoiz and N. Balakrishnan, *J. Phys. Chem. Lett.*, 2022, **13**, 4064.
73 P. G. Jambrina, J. F. E. Croft, H. Guo, M. Brouard, N. Balakrishnan and F. J. Aoiz, *Phys. Rev. Lett.*, 2019, **123**, 43401.
74 V. Sáez-Rábanos, J. E. Verdasco, F. J. Aoiz and V. J. Herrero, *Phys. Chem. Chem. Phys.*, 2021, **23**, 8002.

75 H. da Silva, B. K. Kendrick and N. Balakrishnan, *J. Chem. Phys.*, 2022, **156**, 044305.
76 U. Buck, F. Huisken, G. Maneke and J. Schaefer, *J. Chem. Phys.*, 1983, **78**, 4430.
77 U. Buck, F. Huisken, J. Schleusener and J. Schaefer, *J. Chem. Phys.*, 1981, **74**, 535.
78 R. V. Krems, *TwoBC – quantum scattering program,* University of British Columbia, Vancouver, Canada, 2006.
79 G. Quéméner, N. Balakrishnan and R. V. Krems, *Phys. Rev. A: At., Mol., Opt. Phys.*, 2008, **77**, 30704.
80 G. Quéméner and N. Balakrishnan, *J. Chem. Phys.*, 2009, **130**, 114303.
81 J. P. Ríos, M. Bartolomei, J. C. Martínez, M. I. Hernández and R. H. Lamoneda, *J. Phys. Chem. A*, 2009, **113**, 14952.
82 A. M. Arthurs and A. Dalgarno, *Proc. R. Soc. London, Ser. A*, 1960, **256**, 540.
83 J. Schaefer and W. Meyer, *J. Chem. Phys.*, 1979, **70**, 344.
84 R. N. Zare, *Ber. Bunsenges. Phys. Chem.*, 1982, **86**, 422.
85 N. Mukherjee, W. E. Perreault and R. N. Zare, *Stark-induced adiabatic passage processes to selectively prepare vibrationally excited single and superposition of quantum states*, Elsevier, 2018, p. 1.
86 N. Balakrishnan, R. C. Forrey and A. Dalgarno, *Chem. Phys. Lett.*, 1997, **280**, 1.
87 E. P. Wigner, *Phys. Rev.*, 1948, **73**, 1002.
88 D. D. Fazio, V. Aquilanti and S. Cavalli, *J. Phys. Chem. A*, 2020, **124**, 12.
89 D. D. Fazio, V. Aquilanti and S. Cavalli, *Front. Chem.*, 2019, **7**, 328.
90 D. W. Schwenke, *J. Chem. Phys.*, 1988, **89**, 2076.